A Novel Algorithm for Detection of Convective Initiation Using Multi-Source Satellite Images

Jia Liu[1,2], Qian Zhang[1]*

[1] School of Information Technology, Shangqiu Normal University, China
[2] State Key Laboratory of Mathematical Engineering and Advanced Computing, Zhengzhou Information Science and Technology Institute, China
sqsylj@126.com, sqzyliujia@163.com

Abstract

Severe convective weather is a type of extreme weather characterized by sudden and intense conditions, often featuring heavy short-term rainfall, lightning, strong winds, hail, tornadoes, and other related disasters. The initiation of convection indicates that severe weather is imminent and is essential for short-term forecasting. However, the horizontal movement of clouds can hinder the precision of algorithms designed to detect convection initiation. To address this issue, a novel algorithm utilizing cloud-top rapid cooling rates from multi-source satellite images has been developed. This algorithm leverages the high temporal resolution of the 6-minute fast scan data from the FY-2F satellite and includes a filter with three testing conditions to enhance the accuracy of detecting convective initiation. The algorithm significantly improves detection accuracy by addressing the challenge of horizontal cloud movement, which has been a persistent issue in previous detection methods. By integrating data from infrared, water vapor, and visible light channels, the algorithm provides a comprehensive approach to identifying CI signals in their early stages. This advancement is crucial for enhancing the timeliness and accuracy of short-term severe weather warnings, thereby contributing to more effective disaster prevention and mitigation efforts.

Keywords: Convective initiation, Fast cooling rates, FY-2F satellite, Rapid scan data, Multi-source

1 Introduction

Severe convective weather, which is a form of extreme weather, often causes heavy rainfall, hail, and tornadoes, resulting in significant loss of life and damage to property. It also greatly affects economic development, social progress, and the lives of individuals [1-3]. Convection Initiation (CI) signifies the start of intense convective weather activity, and accurately detecting CI is essential for short-term forecasting of severe convective weather. The importance of CI lies in its capacity to forecast and reduce the potential harm from severe convective weather events [4-5].

A key feature of CI is the quick change in the cooling rate at the top of clouds over a short period. The rapid scan data from the FY-2F geostationary meteorological satellite, which has a six-minute interval and a spatial resolution of 5 km, provides an opportunity for accurate detection of CI. Currently, geostationary meteorological satellites are the main tools for monitoring and analyzing convective weather due to the limited reach of traditional detectors and radar systems [6-8]. These satellites offer high temporal resolution and broad observation capabilities. With ongoing advancements in satellite remote sensing technology, the temporal and spatial resolutions of these satellites have greatly improved compared to earlier predecessors. As a result, research has increasingly focused on using satellite remote sensing to monitor convective weather, particularly in identifying CI and rapidly developing convective (RDC). The goal is to detect signals in the early phases of the convective life cycle, which allows for more accurate and effective predictions [9-11].

CI is defined as the image element on a satellite cloud map that corresponds to the first detection of reflectivity ≥ 35dBz by Doppler weather radar, indicating the presence of convective clouds. The core of the CI technique involves analyzing convective motion [12-13]. The CI technique leverages the high temporal frequency of geostationary weather satellites to monitor rapidly developing convection and detect rainfall systems earlier than ground-based radar, thereby providing timely warnings. In recent years, similar algorithms and techniques have been developed based on the statistical relationship between convection and lightning, allowing for the identification of emerging lightning within 0 to 1 hour, which enhances proximity forecasting capabilities [14-16]. Given the limited coverage of traditional detectors and radar, geostationary meteorological satellites have become the primary tool for monitoring and analyzing convective weather activity.

Currently, numerous research findings have been made utilizing remote sensing methods to monitor CI and RDC [17-19]. To investigate the influence of double low-level jets on CI, [20] conducted convective-permitting simulations with a non-hydrostatic mesoscale model. The main features of this algorithm include a significant bright temperature gradient in the fluid, where the bright temperature at the center of the convection is considerably lower than that at the edges, along with a substantial

*Corresponding Author: Qian Zhang; Email: sqzyliujia@163.com
DOI: https://doi.org/10.70003/160792642025092605006

cooling rate. These two features illustrate the spatial and temporal development patterns of the cloud masses. The primary data for the RDC algorithm is sourced from the MSG satellite, utilizing its five channels for RDC detection. In 2002, [21] conducted extensive experiments with this algorithm, achieving an accuracy of 90% and a false detection rate of just 15%. For rapidly developing convection, the Japan Meteorological Agency created the RDCA detection algorithm [22], which established 13 criteria based on five channels of data from the Japanese MTSAT-1R satellite (with a temporal resolution of 5 minutes) to identify and forecast RDC areas through a four-step process: selecting candidate convective clouds, eliminating horizontal cloud movement, re-detection, and consistency verification. This algorithm successfully detected all four RDC cases in Japan on August 18, 2010, although one was a false alarm. The University of Wisconsin's Convective Initiation (UWCI) algorithm utilized two bright temperature images taken 15 minutes apart to create a fast cooling rate image of cloud tops, passing through seven screening conditions, with the final one meeting the criteria indicating incipient convection [23]. The University of Alabama employs a multispectral detection approach for CI and RDC [24], focusing on extracting eight key indicators from satellite channel data, such as IR cloud top bright temperature, IR multi-channel differences, and trends in IR cloud top bright temperature over time. This algorithm was validated by analyzing 213 convective events that occurred in Europe in 2007, achieving a detection accuracy of 80.75%. Additionally, [25] introduced a new CI nowcasting system called the Rapidly Developed Convection Monitoring System (RDCMS), which utilizes data from the advanced geosynchronous radiation imager on the China Fengyun-4A (FY-4A) satellite.

In conclusion, the existing algorithms for identifying CI utilize high temporal resolution satellite data, taking advantage of the rapid cooling observed at the tops of large CI clouds and recognizing CI through a mix of multi-channel data criteria. Many domestic detection algorithms are modified versions of international algorithms, with thresholds adjusted to fit the specific regional characteristics of China. A crucial aspect of satellite-based CI detection is the requirement for frequent satellite observations, which is supported by the rapid scan capabilities of China's FY-2F geostationary meteorological satellite. The proposed method aims to effectively identify CI and RDC by analyzing the cloud-top cooling rate through multi-channel discrimination using the FY-2F's rapid scan data. Cirrus clouds often affect the effectiveness of the CI detection algorithm. To solve this problem, a cloud-top fast cooling rate-based convective initiation detection algorithm was developed. Unlike previous studies that primarily rely on single-channel data or lower temporal resolution, this study introduces a novel algorithm that integrates FY-2F satellite's 6-minute rapid scan data and multi-channel information to address the challenge of horizontal cloud movement, thereby enhancing CI detection accuracy.

2 Data and Methods

2.1 Satellite Data

The data of four channels, namely IR1 (10.3~11.3μm), IR2 (11.5~12.5μm), IR3 (6.3~7.6μm) and VIS (0.55~0.90μm), from FY-2F satellite were utilized to initially filter out warm clouds, cirrus clouds, and thin clouds that could impact detection accuracy (Table 1). The initial filtering process uses a threshold method, primarily eliminating temperature values above 280K for the IR1 channel (indicating warm clouds), above 2K for the IR1-IR2 channel (indicating cirrus clouds), and reflectivity values below 0.45 for the VIS channel. This preliminary filtering is essential for enhancing the accuracy of cloud detection.

Table 1. Wavelength and spatial resolution of FY-2F satellite imager radiometric channels

Channel	Wavelength (μm)	Spatial resolution (km)	Used
IR1	10.3-11.3	5	√
IR2	11.5-12.5	5	√
IR3	6.3-7.6	5	√
IR4	3.5-4.0	5	
VIS	0.55-0.90	1.25	√

2.2 Preliminary Filtering

To better grasp the concept of CI, an example is chosen to showcase its particular development process. As shown in Figure 1, the bright white region signifies CI, while the leftmost IR grayscale image in the top row depicts CI during its initial life cycle phase. It is noticeable that the bright temperature of CI gradually diminishes, resulting in an increase in brightness over time. At the same time, the area slowly expands.

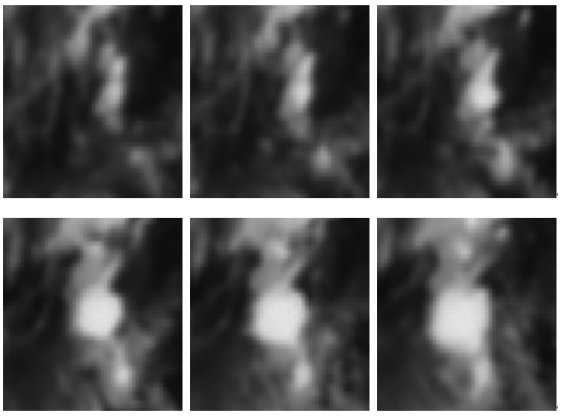

Figure 1. Illustration of CI development process

Assuming that the size of the image I is m × n, the initially filtered image can be defined as

$$I_f = I - I_w - I_c - I_v \quad (1)$$

where Iw represents the warm cloud region, Ic represents the cirrus region, and Iv represents the area where the reflectance of VIS channel which is less than 0.45.

The cloud pixel mean filter was employed to compute the average bright temperature of the cloud pixels within a window that meets the preliminary filtering criteria. The time interval between two consecutive images, I_1 and I_2, is 12 minutes, and the window size is 5x5 pixels, corresponding to an actual distance of 25x25 kilometers given a resolution of 5 kilometers. The fundamental principle of mean filtering is to replace the gray value of each pixel point in an image with the average of the gray values of several neighboring pixel points. Given an image with a gray value of I(m,n), a window neighborhood designated as S_{mn}, and a window containing W points, the mean-filtered image f(m,n) can be expressed as:

$$f(m,n)=\frac{1}{W}\sum_{(x,y)\in S_{mn}} I(x,y) \tag{2}$$

Figure 2 depicts the schematic diagram for the preliminary filtering of two sequential images. Specifically, Figure 2(a) displays the grayscale image of the IR1 channel at 2312 UTC on August 1, 2013, while Figure 2(b) shows the grayscale image of the same channel at 2324 UTC on the same date. Given the short interval between the two images, they are very similar, with only slight variations in cloud size and shape. Figure 2(c) depicts the filtered image derived from Figure 2(a), and Figure 2(d) shows the filtered image corresponding to Figure 2(b).

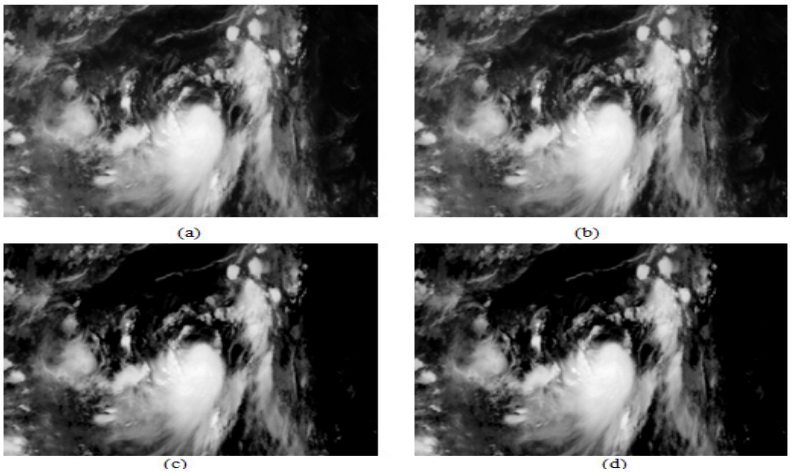

Figure 2. Preliminary filtering of two images: (a) IR1 channel grayscale image at 2312 UTC on August 1, 2013; (b) IR1 channel grayscale image at 2324 UTC on August 1, 2013; (c) Preliminarily filtered image of (a); (d) Preliminarily filtered image of (b)

Subsequently, the difference between the filtered image $f(m,n)$ at the current moment and the filtered image $f'(m,n)$ at the previous moment (12 min ago) is utilized to derive the Cloud-Top Cooling rate (CTC) image. CTC is defined as the difference in cloud-top brightness temperature between consecutive time steps

$$\mathrm{CTC}=f(m,n)-f'(m,n) \tag{3}$$

2.3 CTC Filter

The CTC filter aims to identify regions in the CTC image that satisfy specific criteria. If a region fails the test, it is classified as a CI region. The CTC filter includes three assessments. The three testing conditions are implemented as follows: (1) Limiting horizontal cloud movement: This condition is enforced by calculating the cloud-top brightness temperature change rate between consecutive images. (2) Restricting cold cloud advection toward warm submatrices: This condition involves analyzing the spatial distribution of cloud-top brightness temperatures to identify local minima. (3) Filtering based on CI discrimination criteria: This condition combines data from IR1, IR2, and IR3 channels to apply a set of thresholds that distinguish CI regions from non-CI regions. Subsequently, filtering is carried out according to the CI discrimination criteria.

Figure 3 depicts the CTC image. The presence of non-zero image elements can be attributed to two factors: (1) The vertical development of the cloud that has not yet matured, necessitating retention; (2) The horizontal movement of the cloud, where a region that was previously cloud-free may have cold clouds in the next moment, resulting in errors that must be corrected.

Figure 4 clearly shows that when the average bright temperature is at or below 225K, the variations in bright temperature across the IR1, IR2, and IR3 channels are minimal. In particular, the bright temperature differences between IR1 and IR3 range from -5.5K to -2.5K, while the difference between IR1 and IR2 spans from -2.4K to -1.6K. These slight variations in bright temperatures indicate a more stable convection pattern.

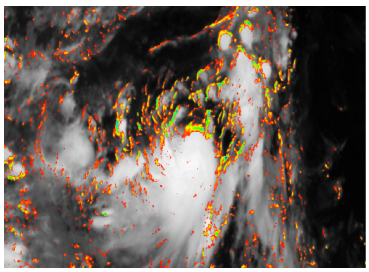

Figure 3. Display of the CTC image superimposed on the original image after subtracting the two images (with color stretching applied)
(The bright temperature difference ranges from -71K to -2K, with red indicating the lowest temperature difference and green indicating the highest.)

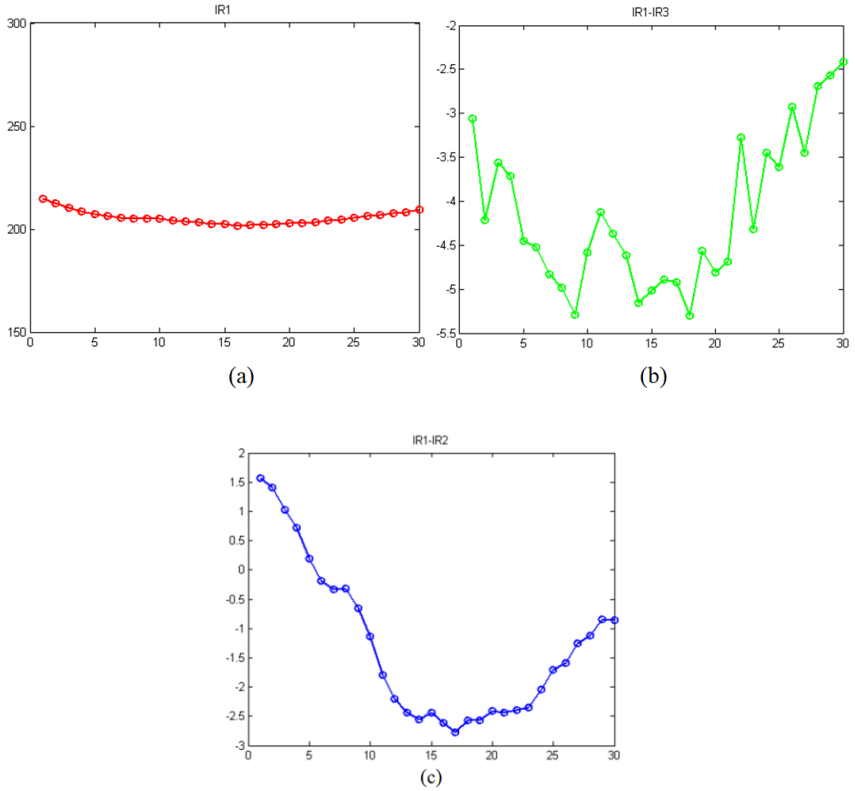

Figure 4. Statistical results of the average bright temperature less than or equal to 225K: (a) IR1 channel; (b) IR1-IR3; (c) IR1-IR2

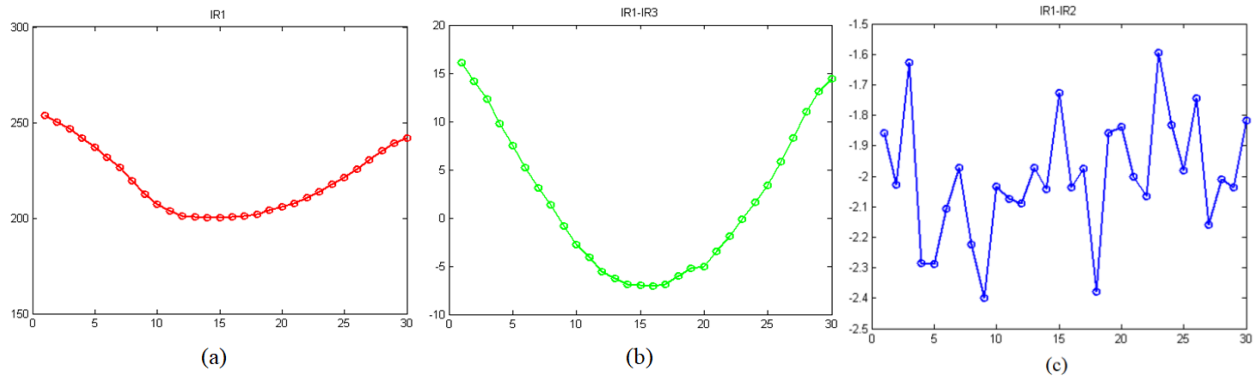

Figure 5. Statistical results for average bright temperature greater than 225K: (a) IR1 channel; (b) IR1-IR3; (c) IR1-IR2

2.4 CI Discernment Conditions

Figure 5 presents statistics of the average bright temperature exceeding 225 K. The temperature difference between IR1 and IR3 varies from -10 K to 20 K, whereas the difference between IR1 and IR2 ranges from -3 K to 2 K. This notable variation in temperature indicates that convection activity occurs frequently.

Based on the statistics and analysis results, four CI discernment conditions were established (Table 2). For regions with an average bright temperature exceeding 225K, the following conditions must be met: 0K < M_IR1-M_IR3 < 35K, 0K < M_IR1-M_IR2 < 3K, VM_IR1-VM_IR3 (rate of change of IR1-IR3) < -1K, and M_IR1 < 243K to account for the low bright temperature in convective regions. For regions with an average bright temperature of 225K or below, CI within the mesoscale convective system (MCS) is indicated when M_IR1-M_IR3 < 0K and M_IR1-M_IR2 < 0K.

Figure 6(a) shows the filtered effect of the CTC filter test1; (b) illustrates the restraining effect of test2; (c) presents the filtered effect of the test3 discriminant condition. The image elements marked with red circles indicate the local minimum temperature points of CI.

Table 2. CI discernment conditions

Discernment conditions	M_IR1−M_IR3	M_IR1−M_IR2	VM_IR1−VM_IR3	M_IR1
M_IR1>225K	(0K,35K)	(0,3K)	(−∞, −1K)	(-∞, 243K)
M_IR1≤225K	(-∞,0K)	(-∞,0K)	N/A	N/A

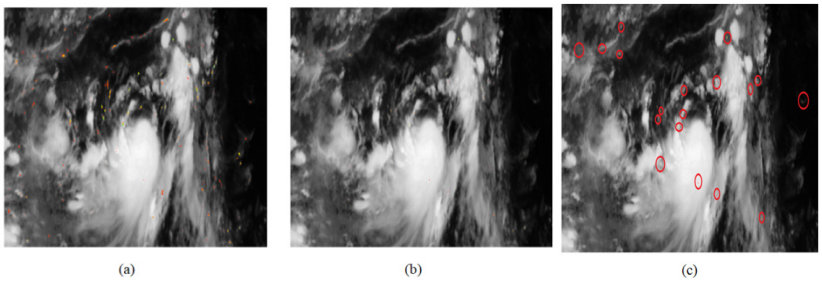

Figure 6. Images after passing three tests in the CTC filter in sequence: (a) Image after test1; (b) Image after test2; (c) Image after test3 (red circles indicate CI bright temperature minima points)

The specific procedure of the proposed algorithm is as follows.

Algorithm. Detection of Convective Initiation (DCI) using multi-source satellite images

Input: IR1 channel adjacent moment grayscale images I1, I2
Output: Incipient convection CI
Step 1: Initialization. Bright temperature threshold T_b, Extended maximum transformation threshold *th* is set to 0.03.
When Tb>241K
Tb← 0
until the end.
Step 2: Initial filtering of I1, I2.using $I_f = I - I_w - I_c - I_v$.
Step 3: The mean filtering of I1, I2 is performed using
$f(m,n) = \frac{1}{W} \sum_{(x,y)\in S_{mn}} I(x,y)$.
Step 4: Differentiate the two images before and after to get the CTC images, $\mathrm{CTC} = f(m,n) - f'(m,n)$.
Step 5: Remove the horizontal movement of the clouds.
Step 6: Reject the cold cloud advection to the warm submatrix and obtain the local bright temperature minimum image element.
Step 7: Combine the IR1, IR2 and IR3 channels for filtering according to the CI discrimination conditions in Table 1.
Step 8: Use the EMTRG algorithm to fill the fluid.

3 Results and Discussion

The validation of the algorithm's performance was conducted using a comprehensive dataset comprising 150 CI events observed over a two-year period. The dataset was carefully curated to include a diverse range of meteorological conditions, cloud types, and geographical locations to ensure the results' generalizability.

3.1 IR Channel

In our earlier research, the EMTRG algorithm was employed to fill the convective cells region of CI identified by the proposed DCI algorithm [26]. The EMTRG algorithm first detected the convective cells and then filled in the local bright temperature minima of CI that had successfully passed the three tests mentioned earlier. Figure 7 illustrates the CI detection results on the IR1 grayscale image, showing both the detection outcomes and the locations of CIs, with the filled convective cell regions marked in blue. Notably, a total of 18 CIs were identified in this instance, which corresponds to the number of CI local bright temperature minimum points found by test3 in Figure 6(c). Both figures indicate a count of 18. The results indicate that the DCI algorithm is effective in detecting CI. The IR channel effectively detects cloud-top cooling but is less sensitive to low-level convection.

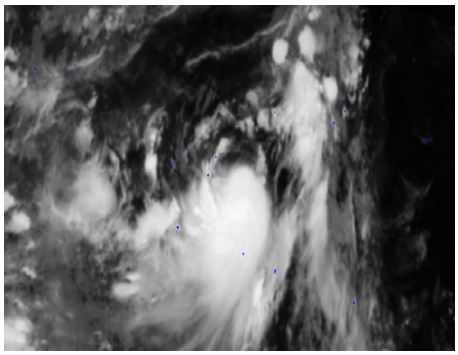

Figure 7. Results of DCI method, the blue part is the region of convective cells where CI is located

3.2 Water Vapor Channel

The image sequences from the water vapor channel (IR3) were selected for experiments on CI detection. To assess the proposed algorithm's effectiveness, the results were compared with those obtained from the IR1 channel image sequence. The chosen image sequences are from the water vapor channel at 0000UTC and 0100UTC on May 19, 2015, with a one-hour interval and a spatial resolution of 5 km.

Firstly, the threshold method was applied to perform preliminary filtering, removing warm clouds, cirrus clouds, and thin clouds that could disrupt the detection process. Secondly, a mean filtering of cloud pixels was performed, which involved calculating the average bright temperature for all cloud pixels within a 5×5 pixel window that satisfied the preliminary filtering criteria. Thirdly, the difference between the filtered image at the current time and the previous time was computed to create the CTC image. Fourthly, The CTC filter was then evaluated using the same approach as the IR1 channel.

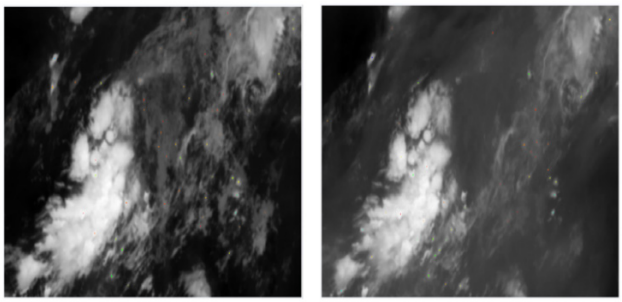

(a) (b)

Figure 8. Filtering results based on CI discrimination conditions (colored points represent local bright temperature minima): (a) IR1 channel results; (b) IR3 channel results

Figure 8 illustrates the results after filtering based on the CI discrimination criteria, with the colored area representing the minimum bright temperature point. It is evident that the IR1 channel identifies bright temperature minima compared to the water vapor channel, highlighting the unique characteristics of the water vapor channel. Since primary convective water vapor is limited, the water vapor channel is not able to effectively detect primary convection. The water vapor channel offers advantages in detecting high-level convection but struggles with low-level detection.

Finally, by incorporating the EMTRG algorithm, the local bright temperature minima of CI that have successfully undergone the three tests mentioned earlier are filled with the regions of convective cells identified by the proposed algorithm. As depicted in Figure 9, the blue area indicates the filled regions of convective cells.

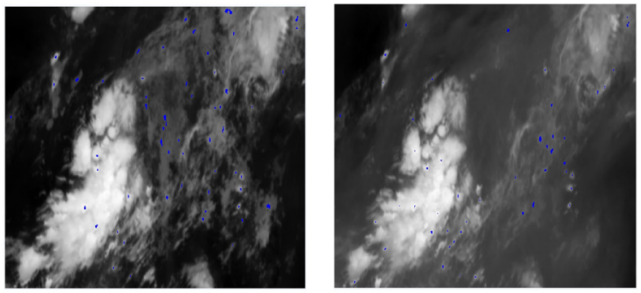

(a) (b)

Figure 9. Comparison of CI detection results for IR1 channel and water vapor channel: (a) Results of IR1 channel; (b) Results of water vapor channel

3.3 VIS Channel

The performance of the proposed algorithm was evaluated using visible channel data from the FY-2F satellite, which has a spatial resolution of 1 km. The selected case study focuses on the image sequence captured between 0106-0506UTC on August 2, 2013, with a two-hour interval between VIS images. The high resolution of the VIS channel provides a clearer view of convective cloud textures, allowing for more precise observation of CI detection results compared to the IR channel. Figure 10 offers an initial visualization of CI locations and shows that CI can occur either individually or as part of an MCS. A total of 36 CI cases, indicated as blue areas, were identified in these three VIS sequence images, demonstrating high detection accuracy and a low false alarm rate. The VIS channel provides higher spatial resolution for clearer cloud textures but is limited by daylight conditions.

3.4 Statistical Analysis

To provide a comprehensive evaluation of the algorithm's performance, we conducted a detailed statistical analysis using a dataset of 150 CI events. The analysis included the calculation of several key metrics:

Precision: The ratio of true positive detections to the total number of positive detections (including false alarms).

Recall: The ratio of true positive detections to the total number of actual CI events.

The results showed that our algorithm achieved a precision of 82%, and a recall of 77%. These metrics indicate that the algorithm effectively balances the trade-off between minimizing false alarms and maximizing detection accuracy. This analysis reinforces the algorithm's reliability and effectiveness in real-world applications.

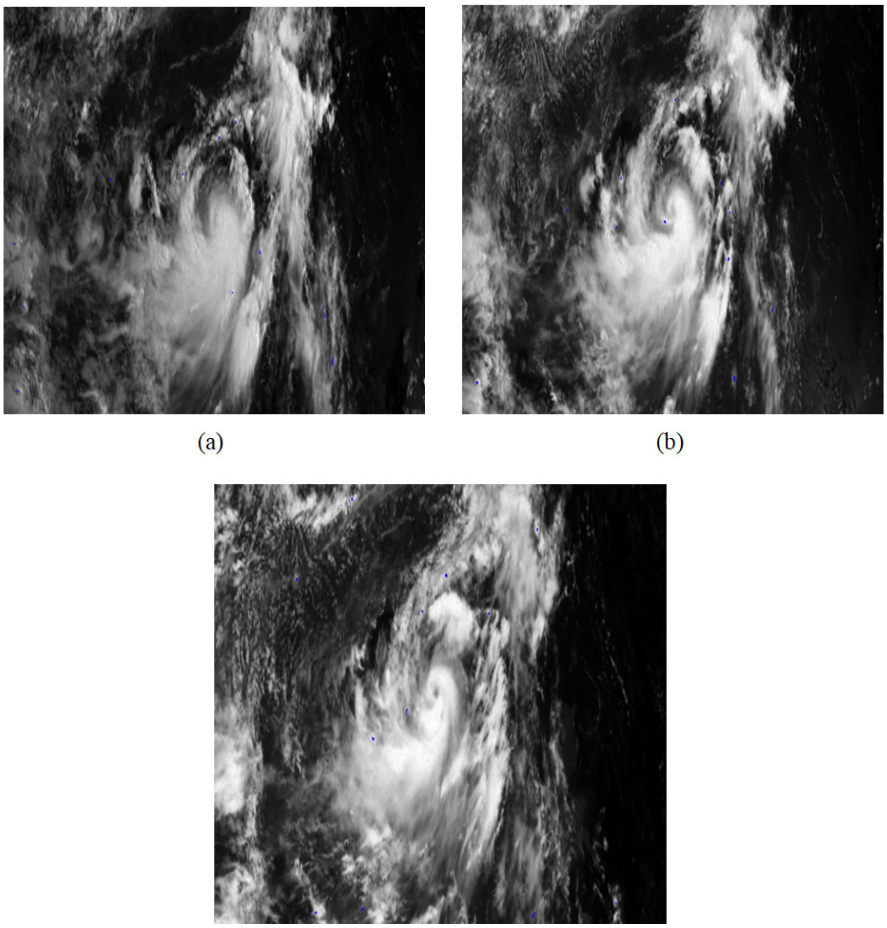

Figure 10. CI detection results of the proposed DCI algorithm on visible channel sequence images (depicted in blue): (a) Detection results of VIS channel at 0106UTC, August 2; (b) Detection results of VIS channel at 0306UTC, August 2; (c) Detection results of VIS channel at 0506UTC, August 2

4 Conclusion

A new algorithm for detecting convective initiation, called DCI, has been developed using images from the FY-2F satellite. This algorithm takes advantage of the satellite's high temporal resolution, which provides fast scan data every 6 minutes, and the rapid cooling rate of cloud tops. The threshold method is employed for initial filtering to remove warm, cirrus, and thin clouds. Furthermore, a CTC filter with three specific test conditions is implemented to improve the accuracy of CI detection. The algorithm's design prioritizes computational efficiency and modularity to ensure its viability for real-time implementation in operational weather forecasting systems. To further enhance real-time performance, we have implemented several software optimizations, including parallel processing of image data and efficient memory management techniques. The effectiveness of this algorithm is validated through comparison experiments with both the water vapor and VIS channels. This study's main contribution is the development of a novel CI detection algorithm using multi-source satellite images, which significantly enhances detection accuracy and warning lead time. Future work will integrate machine learning techniques to further optimize algorithm performance and explore broader meteorological applications.

Acknowledgment

The authors thank the National Satellite Meteorological Centre (NSMC) of China for providing satellite images. This research was funded by the Science and Technology Department of Henan Province (grant number 242102210078), Key Scientific Research Project of Colleges and Universities of Henan Province (grant number 25A520054) and Foundation of Henan Young Cadre Teachers (grant number 2024GGJS115).

References

[1] L. Wang, Y. Dong, C. Zhang, Z. Heng, Extreme and severe convective weather disasters: A dual-polarization radar nowcasting method based on physical constraints and a deep neural network model, *Atmospheric Research*, Vol. 289, Article No. 106750, July, 2023.

https://doi.org/10.1016/j.atmosres.2023.106750

[2] R. Ma, J. Sun, X. Yang, A 7-yr climatology of the initiation, decay, and morphology of severe convective storms during the warm season over North China, *Monthly Weather Review*, Vol. 149, No. 8, pp. 2599-2612, August, 2021. https://doi.org/10.1175/MWR-D-20-0087.1

[3] X. Zhang, J. Sun, Y. Zheng, Y. Zhang, R. Ma, X. Yang, K. Zhou, X. Han, Progress in severe convective weather forecasting in China since the 1950s, *Journal of Meteorological Research*, Vol. 34, No. 4, pp. 699-719, August, 2020. https://doi.org/10.1007/s13351-020-9146-2

[4] Y. Du, G. Chen, B. Han, C. Mai, L. Bai, M. Li, Convection initiation and growth at the coast of South China. Part I: Effect of the marine boundary layer jet, *Monthly Weather Review*, Vol. 148, No. 9, pp. 38473869, September, 2020. https://doi.org/10.1175/MWR-D-20-0089.1

[5] Q. Sun, A. Abulikemu, J. Yao, A. Mamtimin, L. Yang, Y. Zeng, R. Li, D. An, Z. Li, A Case Study on the Convection Initiation Mechanisms of an Extreme Rainstorm over the Northern Slope of Kunlun Mountains, Xinjiang, Northwest China, *Remote Sensing*, Vol. 15, No. 18, Article No. 4505, September, 2023. https://doi.org/10.3390/rs15184505

[6] R. K. Giri, S. Prakash, R. Yadav, N. Kaushik, M. V. Shukla, P. K. Thapliyal, K. C. Saikrishnan, A review of the global operational geostationary meteorological satellites, *Remote Sensing Applications: Society and Environment*, Vol. 37, Article No. 101403, January, 2025. https://doi.org/10.1016/j.rsase.2024.101403

[7] R. Ji, Q. Liu, Y. Zhang, X. Liu, A New Improved Method of Recurrent Memory Perception for Radar Echo Extrapolation, *2024 IEEE 24th International Conference on Software Quality, Reliability, and Security Companion*, Cambridge, United Kingdom, 2024, pp. 779-785. https://doi.org/10.1109/QRS-C63300.2024.00104

[8] S. Tao, Q. Liu, Y. Zhang, X. Liu, High Intensity Radar Echo Extrapolation Based on Stacked Generative Structure, *2024 IEEE 24th International Conference on Software Quality, Reliability, and Security Companion*, Cambridge, United Kingdom, 2024, pp. 746-751. https://doi.org/10.1109/QRS-C63300.2024.00099

[9] J. R. Walker, W. M. MacKenzie Jr, J. R. Mecikalski, C. P. Jewett, An enhanced geostationary satellite–based convective initiation algorithm for 0–2-h nowcasting with object tracking, *Journal of Applied Meteorology and Climatology*, Vol. 51, No. 11, pp. 1931-1949, November, 2012. https://doi.org/10.1175/JAMC-D-11-0246.1

[10] Y. Li, Y. Liu, Y. Shi, B. Chen, F. Zeng, Z. Huo, H. Fan, Probabilistic convective initiation nowcasting using Himawari-8 AHI with explainable deep learning models, *Monthly Weather Review*, Vol. 152, No. 1, pp. 363-385, January, 2024. https://doi.org/10.1175/MWR-D-22-0216.1

[11] T. Kawabata, G. Ueno, Non-Gaussian probability densities of convection initiation and development investigated using a particle filter with a storm-scale numerical weather prediction model, *Monthly Weather Review*, Vol. 148, No. 1, pp. 3-20, January, 2020. https://doi.org/10.1175/MWR-D-18-0367.1

[12] J. M. Peters, H. Morrison, T. C. Nelson, J. N. Marquis, J. P. Mulholland, C. J. Nowotarski, The influence of shear on deep convection initiation. Part I: Theory, *Journal of the Atmospheric Sciences*, Vol. 79, No. 6, pp. 1669-1690, June, 2022. https://doi.org/10.1175/JAS-D-21-0145.1

[13] T. M. Weckwerth, D. B. Parsons, A review of convection initiation and motivation for IHOP_2002, *Monthly weather review*, Vol. 134, No. 1, pp. 5-22, January, 2006. https://doi.org/10.1175/MWR3067.1

[14] H. Morrison, J. M. Peters, K. K. Chandrakar, S. C. Sherwood, Influences of environmental relative humidity and horizontal scale of subcloud ascent on deep convective initiation, *Journal of the Atmospheric Sciences*, Vol. 79, No. 2, pp. 337-359, February, 2022. https://doi.org/10.1175/JAS-D-21-0056.1

[15] L. Bai, G. Chen, Y. Huang, Z. Meng, Convection initiation at a coastal rainfall hotspot in South China: Synoptic patterns and orographic effects, *Journal of Geophysical Research: Atmospheres*, Vol. 126, No. 24, Article No. e2021JD034642, December, 2021. https://doi.org/10.1029/2021JD034642

[16] M. Hirt, G. C. Craig, A cold pool perturbation scheme to improve convective initiation in convection-permitting models, *Quarterly Journal of the Royal Meteorological Society*, Vol. 147, No. 737, pp. 24292447, April, 2021. https://doi.org/10.1002/qj.4032

[17] L. Bai, G. Chen, L. Huang, Convection initiation in monsoon coastal areas (South China), *Geophysical Research Letters*, Vol. 47, No. 11, Article No. e2020GL087035, June, 2020. https://doi.org/10.1029/2020GL087035

[18] J. M. Peters, H. Morrison, T. C. Nelson, J. N. Marquis, J. P. Mulholland, C. J. Nowotarski, The influence of shear on deep convection initiation. Part II: Simulations, *Journal of the Atmospheric Sciences*, Vol. 79, No. 6, pp. 1691-1711, June, 2022. https://doi.org/10.1175/JAS-D-21-0144.1

[19] O. Branch, A. Behrendt, Z. Gong, T. Schwitalla, V. Wulfmeyer, Convection initiation over the eastern Arabian Peninsula, *Meteorologische Zeitschrift*, Vol. 29, No. 1, pp. 67-77, April, 2020. https://doi.org/10.1127/metz/2019/0997

[20] Y. Du, G. Chen, Heavy rainfall associated with double low-level jets over southern China. Part II: Convection initiation, *Monthly Weather Review*, Vol. 147, No. 2, pp. 543-565, February, 2019. https://doi.org/10.1175/MWR-D-18-0102.1

[21] C. Morel, S. Sénési, F. Autones, Building upon SAF-NWC products: Use of the Rapid Development Thunderstorms (RDT) product in Météo-France nowcasting tools, *Proceeding of the 2002 Meteorological Satellite Data Users' Conference*, Dublin, Ireland, 2002, pp. 248-255.

[22] I. Okabe, T. Imai, Y. Izumikawa, T. Matsumoto, Detection of rapidly developing cumulus areas through mtsat rapid scan operation observations, *Meteorological Satellite Center Technical Note*, Vol. 55, pp. 69-91, February, 2011.

[23] J. M. Sieglaff, L. M. Cronce, W. F. Feltz, K. M. Bedka, M. J. Pavolonis, A. K. Heidinger, Nowcasting convective storm initiation using satellite-based box-averaged cloud-top cooling and cloud-type trends, *Journal of applied meteorology and climatology*, Vol. 50, No. 1, pp. 110-126, January, 2011. https://doi.org/10.1175/2010JAMC2496.1

[24] J. R. Mecikalski, K. M. Bedka, Forecasting convective initiation by monitoring the evolution of moving cumulus in daytime GOES imagery, *Monthly Weather Review*, Vol. 134, No. 1, pp. 49-78, January, 2006. https://doi.org/10.1175/MWR3062.1

[25] F. Sun, D. Qin, M. Min, B. Li, F. Wang, Convective Initiation Nowcasting Over China From Fengyun-4A Measurements Based on TV-L_1 Optical Flow and BP_Adaboost Neural Network Algorithms, *IEEE Journal of Selected Topics in Applied Earth Observations and Remote Sensing*, Vol. 12, No. 11, pp. 4284-4296, November, 2019. https://doi.org/10.1109/JSTARS.2019.2952976

[26] J. Liu, C. Ma, C. Liu, D. Qin, X. Gu, An extended maxima transform-based region growing algorithm for convective cell detection on satellite images, *Remote Sensing Letters*, Vol. 5, No. 11, pp. 971-980, November, 2014. https://doi.org/10.1080/2150704X.2014.980917

Biographies

Jia Liu received the Ph.D. degree from Nanjing University of Science and Technology, China, in 2016. He is currently an associate with the School of Information Technology, Shangqiu Normal University. His research interests include Artificial intelligence, computer vision and remote sensing data processing.

Qian Zhang received the M.S. degree from Jiangxi Normal University, China, in 2011. She is currently a lecturers with the School of Media and communication, Shangqiu Normal University. Her research interests include Internet communication, Artificial intelligence.